Cerâmica. 2024, v.70:eHYQT4154
ORIGINAL ARTICLE
http://dx.doi.org/10.1590/HYQT4154

Fabrication parameters of ZnO jet nebulizer sprayed films: an analysis of morphological, optical and crystalline properties

L. E. Morinigo[1,2,3], D. Richard[1,4], P. Vaveliuk[2,3], M. R. Tejerina*[1,3]

[1]Centro de Tecnología de Recursos Minerales y Cerámica (CETMIC - CIC-CONICET-CCT La Plata-UNLP), Cno. Centenario y 506 s/n, C.C.49 (B1897ZCA), M. B Gonnet, Argentina.

[2]Centro de Investigaciones Ópticas de La Plata (CIOP-CIC-CONICET-CCT La Plata-UNLP) Cno. Centenario y 506 s/n, C.C. 3 (B1897ZCA), M. B Gonnet, Argentina.

[3]Universidad Nacional Arturo Jauretche, Av. Calchaquí 6200 (B1888), Florencio Varela, Provincia de Buenos Aires.

[4]Universidad Nacional de La Plata, Calles 47 y 115 (B1900), La Plata, Buenos Aires, Argentina.

Abstract

This study examines the influence of fabrication parameters on the morphological, optical, and structural characteristics of zinc oxide (ZnO) films prepared using the jet nebulizer spray pyrolysis technique. Specifically, we analyze the impact of the application distance (ranging from 2 to 8 cm), substrate temperature (ranging from 325 to 425 °C), carrier air pressure (ranging from 5 to 15 psi), and the molar percentage of deionized water/ethanol in the precursor solution (ranging from 0 to 25%). Scanning electron microscopy, X-ray diffraction, and optical transmittance spectroscopy are employed for characterization. Under the employed conditions, film thicknesses ranging between 100 and 680 nm, predominantly strong orientation along the 002 crystalline plane, and visible transparency between 70 and 90% are obtained. Additionally, various morphologies are identified and inspected. Particularly, films produced at longer distances, higher temperatures, and using low or moderate water/ethanol ratios exhibit higher visible transparency (90%), a homogeneous morphology devoid of grain overgrowth, and thicknesses up to 200 nm. These features are desirable for photonic and optoelectronic applications, thus motivating further investigations using the employed technique to obtain wider thicknesses while maintaining these target properties. In summary, this work evaluates the feasibility and tunability of producing transparent and homogeneous ZnO films using the low-cost jet nebulizer spray pyrolysis and contributes to the understanding of this growth process.

Keywords: ZnO, jet, nebulizers.

INTRODUCTION

Zinc oxide (ZnO) films hold great promise as transparent conductive oxides owing to their outstanding chemical and thermal stability, wide direct band gap energy (E_g=3.3 eV), and abundant availability [1,2]. This class of materials finds applications in various devices, including solar cells, gas sensors, diodes, and optical filters [3]. Several techniques have been developed for producing these films, including atomic layer deposition, chemical vapor deposition, pulsed laser deposition, radio frequency magnetron sputtering, and sol-gel-based methods [4-6]. Sol-gel techniques have garnered significant attention due to their ability to operate under atmospheric pressure, without requiring stringent conditions or expensive equipment [7-9]. Among sol-gel methods, those employing spray-pyrolysis or pyrolytic nebulization have seen increasing exploration in the past decade [10-13]. The key common feature of these techniques is the generation of droplets from a solution containing the necessary cation for the desired material, which are then deposited onto a heated substrate [14]. Depending on the method used to generate the droplets, these sol-gel techniques can be classified into almost three types: Pneumatic Spray Pyrolysis (PSP), Jet Nebulizer Spray Pyrolysis (JNSP), and Ultrasonic Nebulizer Spray Pyrolysis (UNSP).

In PSP, where pneumatic spraying is the source of the droplets, the precursor solution and pressurized carrier gas are delivered to the atomization nozzle, where the liquid is then sprayed directly onto the substrate using either a manual or automated application system. Several authors have reported the use of an airbrush or spraying gun for this purpose [7,10,11].

In the case of JNSP, the precursor solution, held in a nebulization reservoir, is atomized into fine droplets via the Venturi effect and directed to the substrate through a pipe.

For UNSP, the process is similar to JNSP, but the aerosol or nebulization mist is generated by ultrasonic vibration produced by a piezoelectric device.

While all these processes are cost-effective, environmentally friendly, easily scalable, and capable of producing thin films [10,11,17], significant differences exist between them. PSP, for instance, is the most reported technique for certain parametric variations and different applications. However, it does not allow a gentle carrier gas flow, which is desirable for precise deposition control, and it typically requires a higher consumption of materials [18].

On the other hand, both JNSP and UNSP techniques

* *matiast@cetmic.unlp.edu.ar*
https://orcid.org/0000-0002-0799-7611

Table I - Spray pyrolysis Variants, Characteristics, and Film applications

Technique	Characteristics	Applications
PSP	Well-known deposition conditions, higher carrier gas Flow, higher material consumption, higher droplet size dispersion, Easy nozzle obturation, less repetitively.	Solar cells[22] Gas sensors [23] UV detectors [24] Optical waveguiding [25-27]
JNSP	Smooth Carrier gas Flow, lower material consumption,lower droplet size dispersion, smaller droplet mean size, robust system.	Solar cells [28] Gas sensors [29] Diodes [30]
UNSP	Limited deposition time because of overheating, higher droplet size control, smaller droplet mean size.	Solar cells [31] Gas sensor [32] Optical waveguiding [33] Antibacterial coatings [34]

allow for a gentle carrier gas flow and better deposition control, as previously mentioned, but they differ due to the physical mechanisms underlying each nebulization process [19]. Differences in droplet size, temperature variation, and sol concentration during mist generation exist between these techniques, influencing the film growth process [20, 21].

The characteristics of these methods and the typical applications of the films they produce are summarized in Table I.

Regarding the use of these techniques for producing ZnO films, the achieved characteristics depend on the method employed and on various growth variables such as application distance, substrate temperature, carrier gas pressure, and solvent composition, among others [35-37]. In the literature, several studies have explored the impact of varying growth parameters on film properties. For PSP, investigations have focused on the influence of solvent composition [35, 36, 38], carrier gas pressure [8], application distance [11, 39], and substrate temperature [15, 40] on the final film properties. Similarly, the effect of substrate temperature has been analyzed for UNSP [12] and JNSP [16]. However, there is limited information available regarding parametric variations in JNSP.

Furthermore, to our knowledge, the impact of solvent composition (deionized water/ethanol ratio), application distance, and gas carrier pressure on film properties produced by JNSP has not been extensively studied. Optimization of these JNSP parameters according to desired film features is a crucial aspect of the manufacturing process, often requiring iterative experimentation due to the scarcity of published information at this stage [16]. Additionally, previous works in the field have generally overlooked the characterization of coverage area and macroscopic images of resulting films and their relationship with other film properties. This information is essential for film growth assessment, process evaluation, and ensuring repeatability.

Moreover, a current challenge in engineering ZnO film growth is to develop a cost-effective sol-gel process capable of producing thick, high-quality films [41]. These films are desirable for various optoelectronic and photonic devices, including 2D diodes, electrodes, solar cells, and optical waveguides [42-44]. Achieving epitaxial growth is crucial [45], and target films should be composed of compact and homogeneous crystalline grains without overgrowth to ensure surface electronic contact and minimize crystalline defects [46]. Additionally, characteristics such as a visible transparency of around 90% and a controllable thickness of up to approximately 1 μm are highly desirable [27].

In this study, we present an analysis of ZnO film features after producing variations on the fabrication parameters in the JNSP technique. The evaluated parameters include application distance, substrate temperature, air carrier pressure, and solvent composition. The film properties are assessed using scanning electron microscopy (SEM), X-ray diffraction (XRD), UV-VIS-NIR transmittance spectroscopy, and macroscopic images of the films. The obtained results provide valuable insights for optimizing the growth conditions of ZnO films tailored to specific applications and, notably, represent a crucial initial step toward achieving thick, high-quality ZnO films.

MATERIALS AND METHODS

Raw Materials

The starting solution was prepared by dissolving zinc acetate dihydrate ($Zn(CH_3CO_2)2•2H_2O$, Biopack, 99% purity) precursor in absolute ethanol (Biopack, 99% purity) with varying proportions of deionized water (99.9% purity). A small quantity (5 drops) of acetic acid (Biopack, 99% purity) was added to enhance the solubility of the reagent salt. The resulting mixture, with a zinc concentration of 0.1 M, was stirred at room temperature for 20 minutes until a clear and homogeneous solution was achieved.

Characterizations

The morphology of the samples was examined using Scanning Electron Microscopy (SEM, FEI Quanta 200) under high vacuum conditions and at 20.00 kV. The crystalline structure was analyzed by X-ray diffraction (XRD, Bruker D2 Phaser instrument) with a 2θ range from 20 to 70° and steps of 0.02° with a duration of 1 s. Optical properties were investigated by UV-VIS-NIR transmittance spectroscopy using an Agilent 8453 HP spectrophotometer across a wavelength range of 200 to 1200 nm. Subsequently, the computation of the theoretical transmittance spectrum allowed an estimation of the film thickness as previously reported by our group [14], and the bandgap (E_g) was determined using the Tauc relation [47].

Films Set up Preparations

Films were grown using a JNSP system as illustrated in Figure 1. A standard nebulizer device with a 10 ml solution capacity (tank D in the figure) was connected to a compressed air line, and the nebulized droplets were directed toward the substrate through a polypropylene pipe (E) with a 20 mm internal diameter. The spray application was continuous over time, with no relative movement between the mist pipe and the substrate (E and G in the figure, respectively). The substrate holder and mist pipe ends were enclosed within a transparent acrylic cabin (I) within a fume hood. Commercial soda-lime microscope slides (dimensions 2x7x0.1 cm) were used as film substrates. Before each growth process, the substrate was cleaned sequentially with a detergent solution, deionized water, ethanol, and acetone, and dried using compressed air. The substrate (G) was then placed on a heating plate (H) (OHAUS, model e-G51HP07C).

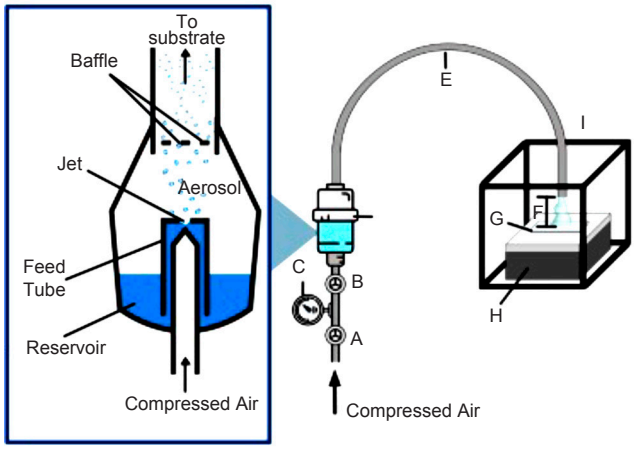

Figure 1: Scheme of the system is employed for films growth, where the following parts are demarcated: (A) pressure knob, (B) compressed air valve, (C) manometer, (D) nebulizer (E) mist pipe, (F) application distance, (G) substrate, (H) heating plate, and (I) acrylic cabin.

The growth parameters were varied as follows: for Series I, the application distance (marked as F in Fig. 1) ranged from 2 to 8 cm; for Series 2, the substrate temperature was varied from 350 to 425°C; for Series 3, the carrier air pressure (see inset Fig.1) was adjusted from 5 to 15 psi; for Series 4, the molar ratio between deionized water and ethanol ranged from 0 to 25%. Freshly prepared solutions were used for all the films. The conditions for each Series are specified in Table II. Additionally, the duration of each film manufacturing process is indicated as growth time. After the specified duration, 10 ml of solution was completely nebulized over the substrate. The carrier air pressure represents the nebulization pressure and is marked in the jet nebulizer scheme inset Figure 1. This pressure was measured using the manometer (C) when the air valve (B) was open.

RESULTS

Series I: Effect of application distance

SEM micrographs showing film morphologies produced at application distances ranging from 8 to 2 cm are presented in Figures 2(a) to 2(e). All observed morphologies at the microscale are practically crack-free, and two distinct appearances can be identified. For the sample produced at 8 cm, compact morphology predominates, characterized by near-circular small grains with a diameter of approximately 20 nm (indicated by A in the figure). Interspersed among these small grains are larger platelets measuring around

Table II. Parameters used for each Series of films; in all the precursor solutions the molarity of Zn is 0.1.

Data Series	Distance (cm)	Temperature (°C)	Carrier air pressure (psi)	Solvent composition (H_2O/C_2H_6O%)	Growth time (min)	Mist flow rate (ml/s)
Series I	2, 3.5, 5, 6.5, 8	400	5	25	40	15
Series II	3.5	325, 350, 375, 425	5	25	40	15
Series III	3.5	375	5, 10, 15	25	40, 10, 7	15, 25, 48
Series IV	3.5	375	10	0, 6, 12, 18, 25	5, 7, 10, 10, 10	25

400 nm in size (indicated by B). Conversely, for samples produced at distances below 6.5 cm, bright elongated structures with dimensions of about 250 x 20 nm were observed (indicated by D), along with a background formed by platelets with dimensions of about 250 nm (indicated by E) and small grains (F).

Detailed close-ups depicting the morphologies of samples produced at 8 cm and 2 cm are provided in Figures 2(f) and 2(g), respectively. Comparing the morphologies described, it can be inferred that the first morphology corresponds to an early stage of film growth, characterized by a lower amount of deposited material due to the small and compacted grains on the surface. In contrast, the second morphology indicates a more advanced stage of the growth process, as evidenced by its more disordered surface due to the presence of various types of grain structures not parallel to the surface.

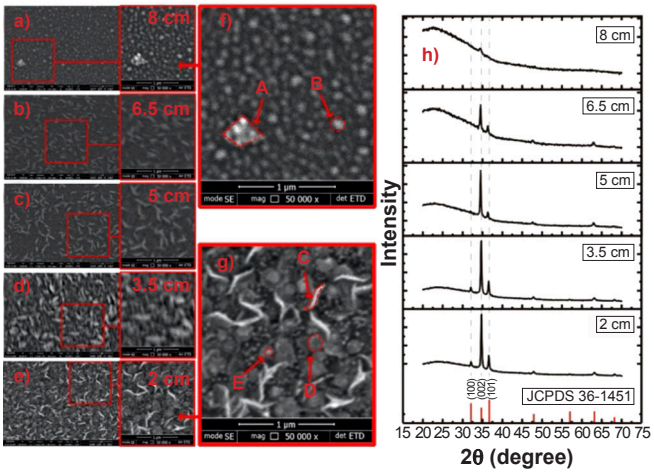

Figure 2: SEM images and XRD patterns for films produced using application distances in the range 2 to 8 cm. Micrographs correspond to application distances of (a) 8 cm, (b) 6.5 cm, (c) 5 cm, (d) 3.5 cm, (e) 2 cm, and close-up views for the cases (f) 8 cm and (g) 2 cm. The corresponding XRD patterns are in (h) together with the crystalline peaks according to JCPDS card No. 36-1451.

The XRD patterns presented in Fig. 2(h) reveal the characteristic hexagonal wurtzite crystal structure typical for ZnO. In this respect, Fig. 2(h) also includes the reflections of the polycrystalline ZnO powder taken from the JCPDC card 36-1451. Within the 2θ range from 30 to 40°, three prominent peaks are observed: the 001-peak at 31.75°, the 002-peak at 34.35°, and the 101-peak at 36.25° [49]. In the obtained patterns, only the [002] peak is weakly observed for the 8 cm sample, while both the 002 and 101 peaks are observed for the 6.5 cm and 5 cm samples. Interestingly, all three peaks mentioned are observed for the 3.5 cm and 2 cm samples. The predominant intensity of the 002 peak in all cases indicates a preferred growth direction along the crystal c-axis in this Series [50].

Figure 3 presents the optical transmittance spectra as a function of wavelength T(λ) for the different application distances, where the different regions are indicated (UV-VIS-NIR). In the UV region, it is observed that greater application distances result in films with higher UV transmittance. This phenomenon is attributed to film thickness: thinner films exhibit reduced propagation distances for absorbed radiation, resulting in decreased absorbance [11,39,46].

The VIS region displays moderate absorption, with no clear correlation observed with application distance. The film produced at the greatest distance exhibits the highest transparency in this region, while the film produced at the intermediate distance of 6.5 cm shows slightly lower transparency. This difference may be attributed to optical scattering caused by variations in film topography [46, 52, 53].

For the NIR region, all transmittance values fall within the range of 75% to 90%, with no significant difference observed in their mean transmittance values.

However, distinct ripples can be identified above λ=500 nm, and these can be utilized to determine the film thickness [7, 51]. To this end, the experimental spectra was compared to simulations of $T(\lambda)$ obtained using the known expression:

$$T(\lambda,s,n,t)= A/(B-C.\cos(\varphi)+D) \quad (A)$$

where $A=16ns^2$, $B=(n+1)^3(n+s^2)$, $C=2(n^2-1)(n^2-s^2)$, $D=(n-1)^3(n-s^2)$, and $\varphi=4\pi nd/\lambda$, being λ the wavelength, *s* is the substrate refractive index (assumed constant and equal to 1.45), n is the film refractive index assumed constant and equal to 1.8 [14] and d is the film thickness. This expression for T(λ) considers that the optical absorptions of substrate and film are negligible [51]. As the product nd determines the transmittance spectral oscillations due to the interference process inside the film, different values of d were set until the ripples of T(λ) matched the experimental measurement.

The optically determined thicknesses for the current Series are 410±10 nm and 480±10 nm for films corresponding to application distances of 2 cm and 3.5 cm, respectively. For the film produced at a distance of 5 cm the thickness is 310±10 nm, for the film produced at 6.5 cm is 210±10 nm, and an undetermined value less than 100 nm is obtained for the film produced at a distance of 8 cm. These results suggest that the amount of material deposited increases as the application distance is reduced. A similar result related to thickness

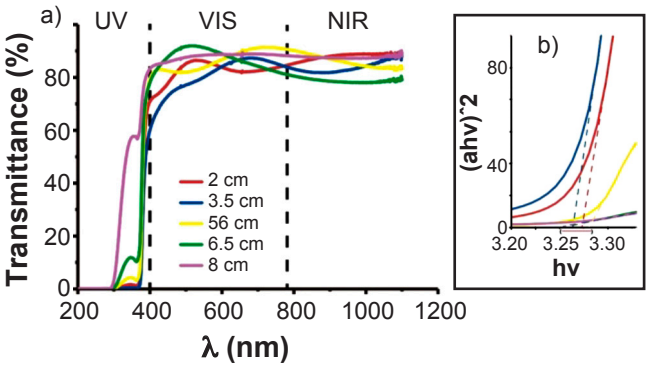

Figure 3: (a) Transmittance spectra for films produced with application distances in the range 2 to 8 cm, and (b) Tauc plots.

variation was recently obtained for spray pyrolysis, but the "nozzle-substrate" distances for this technique can reach up to 30 cm. Moreover, the films obtained in the current work exhibit a higher degree of crystalline orientation and better control of resulting thickness compared to the study [11].

On the other hand, the transmittance spectral region near the threshold wavelength (~380 nm) was utilized to determine the direct bandgap E_g through the Tauc's relation $\alpha h\nu = A_0(h\nu - E_g)^{0.5}$ [20], where hν represents the photon energy, *a* is the absorption coefficient of the film and A_0 is a constant. For all the samples in this Series, it was determined E_g = 3.26±0.02 eV, which shows that the bandgap structure is invariant concerning the variation of this parameter.

Series II: Effect of substrate temperature

SEM micrographs of the films manufactured by varying the substrate temperatures are presented in Figures 3(a-d). The observed morphology for lower temperatures (325 and 350 ºC) differs from that observed for higher temperatures (375 and 425 °C). For temperatures of 325 and 350 ºC, elongated grains of approximately 200 nm in size were observed, which are overlapped and do not exhibit a specific orientation along their normal axes. In contrast, for temperatures of 375 and 425 °C, platelets with sizes of around 250 nm (marked by Ain Fig 4(c)) were observed, oriented perpendicular to the substrate. Additionally, small grains of approximately 10 nm in size (marked by B) and some elongated structures of 200 nm in size (marked by C in Fig 4) were observed. This indicates that increasing the substrate temperature promotes increased mobility of particles during material growth, resulting in a more compact structure.

The XRD patterns for the films in this Series are presented in Figure 4(e). In the XRD patterns for substrate temperatures of 325 and 350 °C all peaks exhibit almost the same intensity (Fig 3c), suggesting a lower degree of preferential crystalline plane orientation. This observation is consistent with the lack of specific orientation of the platelets observed by SEM for this Series. In contrast, a higher intensity of the 002-peak is observed in the XRD patterns when substrate temperatures are 375 and 425 °C, indicating a preferred growth direction along the crystalline c-axis. This finding is consistent with the SEM micrographs of Fig. 4, where a predominant orientation of platelets parallel to the substrate surface is observed.

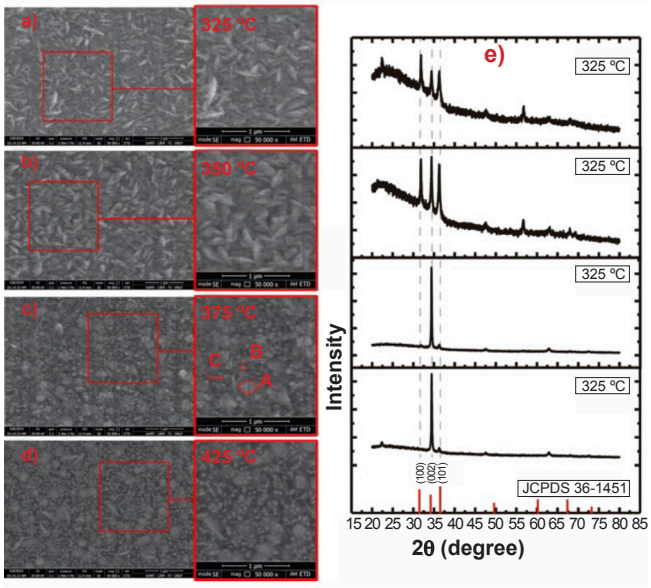

Figure 4: SEM images and XRD patterns for films produced using different substrate temperatures. Micrographs correspond to substrate temperatures of (a) 325°C, (b) 350°C, (c) 375°C, (d) 425°C, with close-up views in all cases and (e) their corresponding XRD patterns.

The optical transmittance spectra for the films in this Series are presented in Figure 5. The transmittance in the UV spectral range is below 1% for all samples in this Series. In the VIS spectral region, the maximum transmittance is obtained for the lowest growth temperature (325ºC, Fig. 3d), reaching a value of about 85%. For higher substrate temperatures (350, 375, and 425 °C), the transmittance in this region is lower, approximately 70% at λ=500 nm, with minor differences (< 5%) between each other. A similar result was obtained in a previous work [12], but higher absorption values were observed for the higher temperatures. This difference can be attributed to a higher water/ethanol ratio employed by them. As will be mentioned in Section 3.4, this ratio affects the absorption of the resulting film. The optically determined thicknesses are 300±10 nm, 380±10 nm, 500±10 nm, and 560±10 nm for the substrate temperatures of 325, 350, 375, and 425 °C, respectively. Finally, a bandgap E_g=3.26±0.02 eV is determined for all the samples in this series.

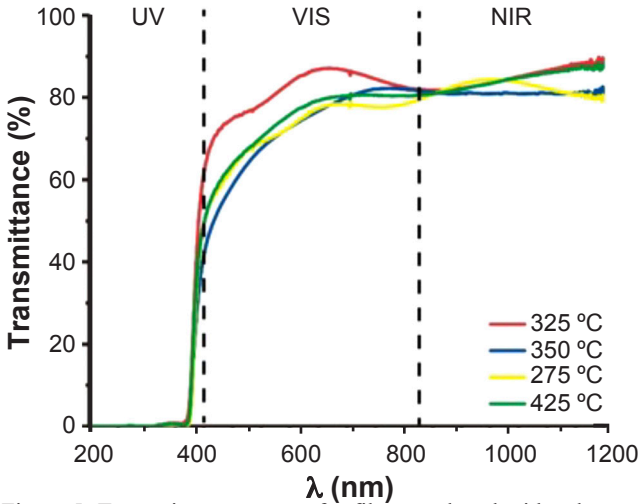

Figure 5: Transmittance spectra for films produced with substrate temperatures in the range 325 to 425 ªC

Series III: Effect of carrier air pressure

SEM micrographs of this Series are presented in Figures 6(a-c). The morphology observed for lower pressures (5 and 10 psi) differs from that observed for 15 psi. For 5 and 10 psi, it is evident that an overgrowth of grains is present,

characterized by elongated grains (marked by A in Fig. 6a) appearing as wedges emerging from the background surface [48]. This background surface is formed by a combination of planar platelets (marked by B in fig.) and small grains (marked by C in fig.). These morphologies resemble those observed in Series I and suggest that the bright elongated grains observed there may be also associated with an overgrowth of grains. In contrast, for 15 psi, the elongated overgrowth grains are not observed. Instead, there is a compact surface composed of grains of different dimensions, similar to the background morphology observed in the previous samples. This indicates that carrier air pressure affects the morphology of the films, in a way that the use of lower pressure results in an overgrowth of grains.

The XRD patterns presented in Figure 4(d) reveal that in all the films of this Series, the intensity of the [002] peak is notably higher than that of the other two peaks corresponding to the 001 and 101 planes. This difference is particularly pronounced for the sample at 15 psi, indicating an increased degree of preferred 002 orientation with higher airline pressure. This observation is consistent with the morphology observed in SEM micrographs, where no overlapped grains were found for the sample at 15 psi.

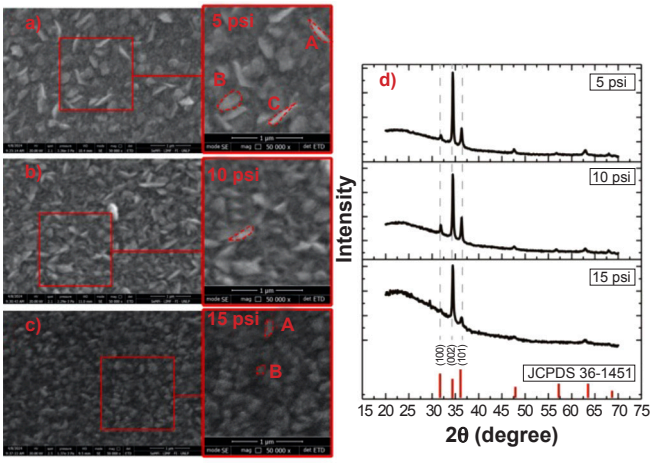

Figure 6: Images were taken by SEM for films produced using different values of the carrier air pressure: (a) 5 psi, (b) 10 psi, (c) 15 psi, and (d) their corresponding XRD patterns.

The transmittance spectra of this Series are presented in Figure 7 and show an increase in the UV and VIS spectral ranges as the pressure increases. In the NIR range, the mean transmittance value does not exhibit significant changes among samples, remaining around 80%. The thicknesses are 680±10 nm, 480±10 nm, and 300±10 nm for the films corresponding to 5, 10, and 15 psi, respectively. Additionally, the computed bandgap is Eg= 3.26±0.02 eV for all the samples in this Series.

The results obtained for this Series indicate an important relationship between the carrier air pressure and film thickness. As the applied pressure increases, significantly thinner films are generated with a predominant 002-crystallographic orientation. This phenomenon can be attributed to the increased velocity of the drops reaching

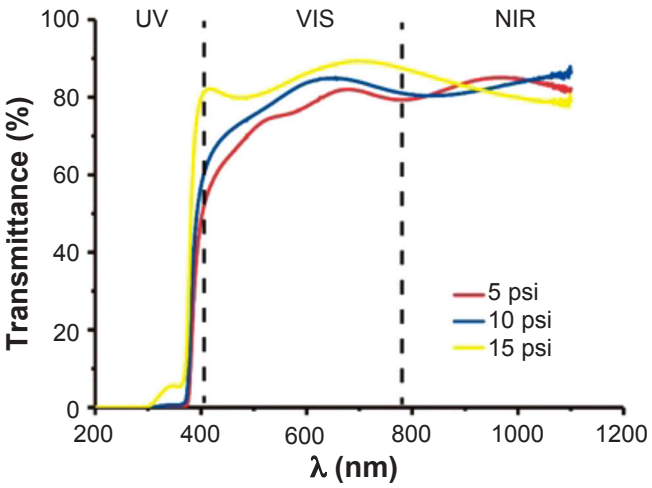

Figure 7: Transmittance for films produced with different values of the carrier air pressure.

the substrate under higher pressure. Consequently, they exhibit stronger bouncing over the substrate and travel further, resulting in thinner films. This effect is analogous to that observed when increasing the application distance, where thickness is also notably reduced. Moreover, the crystallographic texture remains similar for films with similar thicknesses, such as the 5 cm and 15 psi samples. In both cases, the dominant crystallographic orientation persists along the 002-direction, despite the higher growth rate for the 15 psi sample (7 minutes compared to 40 minutes, as indicated in Table II).

Series IV: Effect of solution composition

SEM micrographs of the films manufactured using different water/ethanol molar ratios are presented in Figures 8(a-b). Interestingly, three different morphologies are found depending on the solvent composition. The first prevalent morphology, observed for 0% and 6% water/ethanol ratio, is characterized by homogeneous platelets of about 30 nm (enclosed by the dashed curve in Fig 8(a)). Within this type, the 6% sample exhibits slightly more elongated platelets (marked by A in Fig. 8(b)) and a denser foreground compared to the 0% solvent composition.

The second morphology is observed for the sample produced using a 12% water/ethanol ratio. It presents compact small grains of about 10 nm in the background and larger 500 nm-sized structures over the surface (denoted as B in Fig. 8(c)).

The third morphology, observed for solvent compositions with 18% and 25% water/ethanol ratio, exhibits elongated platelets growing over a background of differently sized grains. This morphology suggests a higher content of water leads to increased overgrowth of the grains and thickness. In this respect, Figures 8(e) and 8(f) present SEM cross section views for the films produced using water/ethanol ratios of 6 and 25%, respectively. From the comparison between these two cases, the later film is thicker than that produced

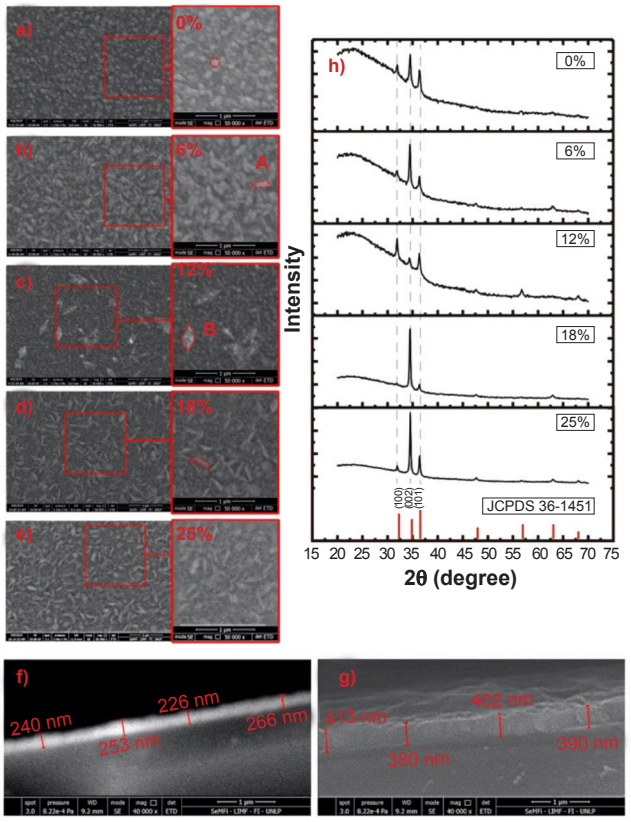

Figure 8: SEM images and XRD patterns for films produced using solutions with different water/ethanol ratios. SEM surface micrographs correspond to ratios of (a) 0%, (b) 6%, (c) 12%, (d) 18%, and (e) 25%, and SEM cross-view are for ratios of (f) 6% and (g) 25%, and (h) their corresponding XRD patterns.

with lower water content (thicknesses are approx. 471 and 265 nm, respectively), and it can also distinguish the grain overgrowth over the surface in the sample produced using the 25% ratio.

The XRD results for this Series are presented in Figure 8(h). The patterns of samples produced with 0, 6, and 12 % water/ethanol ratios present peaks with a weaker intensity in comparison with the glass substrate signal. Within these patterns, 0 and 6% samples show a moderate 002 crystallographic orientation, and the 12% sample is not oriented (the three peaks in the 30-40° 2θ range have practically the same relative intensities as those of the polycrystalline ZnO powder shown in the JCPDC card of Fig 2(h)). In the case of the patterns of 18 % and 25% samples, a strong 002 orientation can be observed. The obtained XRD patterns show that the starting solution composition influences the crystalline structure of the final film, in a way that lower and higher water/ethanol ratios favor moderate and strong 002 crystalline orientation, respectively, while for intermediate ratios no preferential orientation is observed.

Figure 9 presents the transmittance spectra of this Series, and reveals that in the UV spectral region, the sample corresponding to a 0% ratio exhibits transmittance values around 10%, while those corresponding to 6% and 12% water percentage have a UV transmittance curve of about 3%. For 18% and 25% samples, the transmittance drops below 1%. Thus, the UV absorption of the films increases as the water/ethanol ratio in the starting solution is increased. In the VIS spectral region, films corresponding to higher water/ethanol ratios (18% and 25%) present lower transmittance values than those corresponding to lower ratios, with a medium value of 70% at λ= 500 nm. This reduction in transparency in the VIS region also correlates with an increase in the water/ethanol ratio. For the NIR range, the transmittance mean value does not show significant changes between samples, remaining around 80%.

The optically determined thicknesses are 200±10, 285±10, 290±10, 410±10, and 400±10 nm for the films corresponding to 0%, 6%, 12%, 18%, and 25% water content, respectively. This indicates that the thickness of the films increases as the solvent composition is increased, consistent with the reduction in UV transmittance. These thickness measurements agree with those observed through SEM cross-view micrographs in Figs 8(e) and 8(f).

The thickness increase with the solution water content can be explained due to the higher solubility of zinc acetate in water (43 g/100 mL) compared to its solubility in ethanol (3.3 g/100 mL), which along with a longer nebulization duration as the water/ethanol ratio increases (from 5 to 10 minutes, see Table II), results in a larger amount of deposited material for 12%, 18%, and 25% water content.

Finally, a bandgap of E_g= 3.26±0.02 eV is obtained for all the samples in this Series. This result is equal to those determined for all the samples in the other Series and is also in agreement with those reported in the literature for ZnO nebulized films [54].

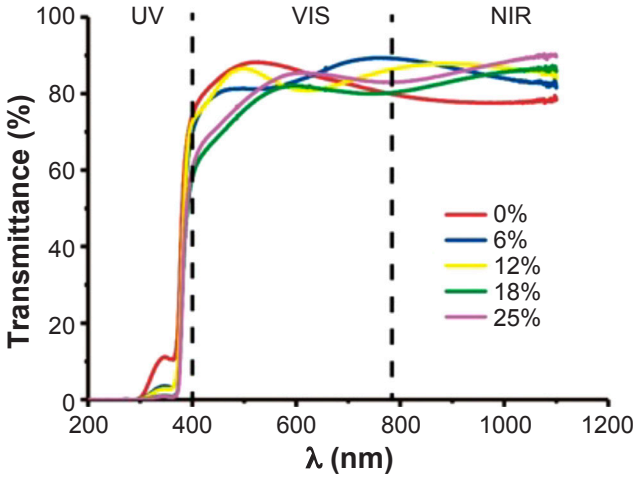

Figure 9: Transmittance spectra for films produced using solutions with different water/ethanol ratios.

General analysis

In the following paragraphs, the most relevant results observed on the studied properties and the relationships between them will be summarized.

The crystalline orientation of the films was primarily influenced by temperature and solvent composition. Higher

temperatures and water/ethanol ratios favored the formation of strongly oriented 002 films, and, other parameters did not significantly affect crystalline orientation under the specified conditions. The UV transparency exhibited a strong dependence on application distance, with greater distances resulting in higher transparency. Conversely, higher air carrier pressure led to a slight increase in UV transparency, while higher water/ethanol ratios slightly decreased transparency. In contrast, VIS transparency showed a strong correlation with air carrier pressure, with higher pressure associated with reduced transparency. Additionally, moderate dependencies on temperature and solvent composition were observed. Increased temperature led to decreased VIS transparency, while higher water content slightly decreased transparency. Closer application distances also resulted in lower VIS transparency.

In regard to film thickness, the variation in application distance showed a significant effect, with a considerable reduction in the film thickness for longer distances. Increasing substrate temperature led to a moderate increase in thickness. Conversely, higher air carrier pressure resulted in reduced thickness, while increasing water content in the solution led to an increase. Overall, these results indicate that the thickness of ZnO films is influenced by various manufacturing parameters, emphasizing the importance of carefully controlling these parameters to achieve the desired thickness.

Another aspect to mention regarding film thickness and the covered area is the film growth process. A frontal macroscopic image of one of the thicker films (approximately 480 nm thick) is presented in Figure 10(a) as a representative example where different color fringes can be identified through naked-eye inspection. The formation of these fringes during the growth process is presented in more detail in Appendix A. The fringes in Fig. 10(a), enclosed by dashed curves, form near-elliptical areas associated with different growth stages. These stages are illustrated in the lower scheme (Fig. 10(b)), where the profile of the film is represented. Initially, the sample starts as a white-colored thin film represented as the white step in Fig. 10(b). As more material is deposited, new fringes appear, which are identified by the different colors they have in the scheme of the figure. Considering the optically measured thickness and the number of fringes, the profile suggests a thickness of about 60 nm for each fringe. Additionally, the film profile represented in Fig. 10 suggests a limit for its maximum height due to the reduction in the area between successive layers under the current experimental conditions. Figure 10(c) shows how it changes the macroscopic appearance of the film and its fringe pattern as the substrate-nozzle distance is increased. The evaluation of the transmittance spectrum in the center (Zone A) and the surrounding (Zone B) of the growth material indicates a different thickness for each zone, for the spectrum of Zone A more nipples and less transparency than that of Zone B can be identified, indicating a wider thickness in the first. This tendency was reproducible for all the samples. Also, for all the Series, an increment in the number of interference fringes agrees with an increment in the optically determined thickness.

Finally, a comprehensive overview of the effect of fabrication parameters is summarized in Table III. Most of the conditions employed result in film thicknesses ranging between 300 and 680 nm. These films exhibit predominantly strong 002 orientation, relatively low visible transparency (approximately 70%), and a morphology characterized by grain overgrowth.

On the other hand, films with thinner thicknesses (rows with bold text in Table III) display strong to moderate crystalline 002 orientation, higher visible transparency (around 90%), and an absence of grain overgrowth. This morphology, along with high VIS transparency and crystalline orientation, represents desirable properties for high-quality films.

Therefore, higher temperatures, increased pressures, lower or moderate water content, and longer application

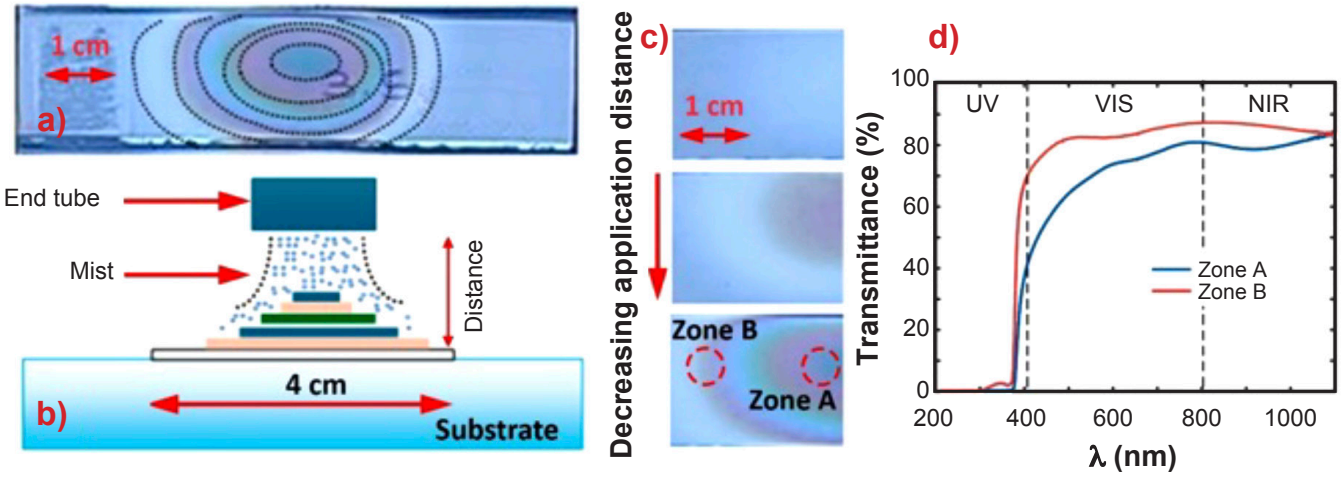

Figure 10: Identification of different grown stages (a) front view image (b) side view scheme(c) macroscopic image of the film coverage area for different substrate-nozzle distance (d) Transmittance spectra of different zones of the growth material.

Table III - *Overview of the effect of the parameters in film properties.*

	Condition	Thickness	Crystalline texture orientation	VIS transparency (approx. value at λ=500 nm)	Grain overgrowth?
Series 1	Long distances	<100 nm	Strong 002	90 %	No
	Short distances	~ 480 nm	Strong 002	75%	Yes
Series 2	Lower temperature	~ 300 nm	Moderate 002	75%	Yes
	Higher temperature	~ 600 nm	Strong 002	75%	Yes
Series 3	Lower pressure	~ 680 nm	Strong 002	70%	Yes
	Higher pressure	~ 300 nm	Strong 002	90%	No
Series 4	Lower H_2O/C_2H_6O %	~200 nm	Moderate and weak 002	90%	No
	Higher H_2O/C_2H_6O %	~400 nm	Strong 002	75%	Yes

distances should be considered as the starting point to produce thicker films while maintaining the grain structure and transparency, aiming for epitaxial growth of ZnO layers.

CONCLUSIONS

In this work, the effect of the fabrication parameters on the growth of ZnO by low-cost jet nebulization spray pyrolysis was deeply investigated. The dependence of morphological, structural, and optical properties on the film fabrication conditions was analyzed, considering the application distance, substrate temperature, carrier air pressure, and solvent composition. Among the obtained results, can be highlighted the following: most of the employed conditions produced films thicker than 300 nm, a morphology with grain overgrowth, the optical transparency of around 70%, and highly 002 crystalline orientated films. Long distances, higher temperatures, and a low or moderate water/ethanol ratio generate films thinner than 300 nm, these are compact films without grain overgrowth, higher visible transparency (90%), and highly crystalline orientation. Then, the last-mentioned fabrication conditions should be employed to produce films for optoelectronic and photonic applications. In future works, multi-step growth processes will be explored to obtain thicker films maintaining these features. In summary, it can be concluded that the obtained results contribute to the knowledge of the target growth process and encourage further work on the research topic.

ACKNOWWLEDGMENTS

The authors want to thank to Ministerio de Ciencia y Tecnología for funding this research work under projects PICT 1994-2014 and PICT 2019-1997.

The authors want to thank Eng. M. Gauna, Lic. M. Ángela Alvarez Manso and Lic. Daniel Díaz Herrera, for their valuable technical support.

REFERENCES

[1] Mote VD, Purushotham Y, Shinde RS, Salunke SD, Dole BN. Structural, optical and antibacterial properties of yttrium-doped ZnO nanoparticles. *Cerâmica*. 2015;**61**:457. doi:10.1590/0366-69132015613601932.

[2] Morais A, Torquato RA, Silva UC, Salvador C, Chesman C. Effect of doping and sintering in structure and magnetic properties of the diluted magnetic semiconductor ZnO . *Cerâmica*. 2018;**64**:627. doi:10.1590/0366-69132018643722463.

[3] Kumawat A, Chattopadhyay S, Misra KP, Misra RDK, Kumari P. Micro-strain governed photoluminescence emission intensity of sol-gel spin coated Eu doped ZnO thin films. *Thin Solid Films*. 2022;**761**:139521. doi:10.1016/j.tsf.2022.139521.

[4] Purohit A, Chander S, Sharma A, Nehra SP, Dhaka MS. Impact of low temperature annealing on structural, optical, electrical and morphological properties of ZnO thin films grown by RF sputtering for photovoltaic applications. *Opt Mater*. 2015;**49**:51. doi:10.1016/j.optmat.2015.08.021.

[5] Exarhos GJ, Sharma SK. Influence of processing variables on the structure and properties of ZnO films. *Thin Solid Films*. 1995;**270**:27. doi:10.1016/0040-6090(95)06855-4.

[6] Tiwari C, Pandey A, Dixit A. Precursor mediated and defect engineered ZnO nanostructures using thermal chemical vapor deposition for green light emission. *Thin Solid Films*. 2022;**762**:139539. doi:10.1016/j.tsf.2022.139539.

[7] Bolino M, Richard D, Tejerina MR. Nickel-doped zinc oxide thin films made by spray pyrolysis: experimental characterization and theoretical analyses. *Cerâmica*. 2023;**69**:107. doi:10.1590/0366-69132023693903431.

[8] Licurgo JSC, de Almeida Neto GR, Paes Junior HR. Structural, electrical and optical properties of copper-doped zinc oxide films deposited by spray pyrolysis. *Cerâmica*. 2020;**66**:284. doi:10.1590/0366-69132020663792877.

[9] Tomakin M, Onuk Z, Rujisamphan N, Shah SI. Role of the radio frequency magnetron sputtered seed layer properties

on ultrasonic spray pyrolyzed ZnO thin films. *Thin Solid Films*. 2017;**642**:163. doi:10.1016/j.tsf.2017.09.039.
[10] Kumar KD, Ganesh V, Valanarasu S, Shkir M, Kulandaisamy I, Kathalingam A, et al. Effect of solvent on the key properties of Al doped ZnO films prepared by nebulized spray pyrolysis technique. *Mater Chem Phys*. 2018;**212**:167. doi:10.1016/j.matchemphys.2018.03.035.
[11] Hafdallah A, Azzedine A, Belhani H, Aida MS, Attaf N. In doped ZnO thin films. *NANO*. 2017;**5**:87. doi:10.1016/j.jallcom.2011.04.058.
[12] Djelloul A, Bouzid K, Guerrab F. Specific signatures of α-alumina powders prepared by calcination of boehmite or gibbsite. *Turkish J Phys*. 2008;**32**:49. doi:10.1016/j.powtec.2010.03.036.
[13] Fiddes A, Durose K, Brinkman A, Coates P, Banister A. Preparation of ZnO films by spray pyrolysis. *J Cryst Growth*. 1996;**159**:210. doi:10.1016/0022-0248(95)00707-5.
[14] Apaolaza A, Richard D, Tejerina MR. Experimental and ab initio study of the structural and optical properties of ZnO coatings: Performance of the DFT+U approach. *Process Appl Ceram*. 2022;**14**:362. doi:10.2298/pac2004362a.
[15] Burgener JA, Makonnen Y. Nebulization systems, in: D. Beauchemin (Ed.), Sample Introduction Systems in ICPMS and ICPOES. *Elsevier*. 2020;57. doi:10.1016/b978-0-444-59482-2.00002-6.
[16] Ravichandran K, Manivasaham A, Subha K, Chandrabose A, Mariappan R. Cost-effective nebulizer sprayed ZnO thin films for enhanced ammonia gas sensing – Effect of deposition temperature. *Surf Interfaces*. 2016;**1-3**:13. doi:10.1016/j.surfin.2016.06.004.
[17] Lehraki N, Aida MS, Abed S, Attaf N, Attaf A, Poulain M. ZnO thin films deposition by spray pyrolysis: Influence of precursor solution properties. *Curr Appl Phys*. 2012;**12**:1283. doi:10.1016/j.cap.2012.03.012.
[18] Gopala Krishnan V, Elango P, Ragavendar M, Sathish P, Gowrisankar G. Effect of doping on the surface modification of nebulizer sprayed BaxZn1−xO nanocrystalline thin films. Mater Res Express. 2017;4:036401. doi:10.1088/2053-1591/aa6077.
[19] Phipps PR, Gonda I. Droplets Produced by Medical Nebulizers. *Chest*. 1990;**97**:1327. doi:10.1378/chest.97.6.1327.
[20] Rahemi Ardekani S, Rouhaghdam AS, Nazari M, Bayat A, Yazdani E, Saievar-Iranizad E. A comprehensive review on ultrasonic spray pyrolysis technique: Mechanism, main parameters and applications in condensed matter. *J Anal Appl Pyrol*. 2019;**141**:104631. doi:10.1016/j.jaap.2019.104631.
[21] Araújo L, Abatti P, Araújo Filho W, Alves RF. Performance evaluation of nebulizers based on aerodynamic droplet diameter characterization using the Direct Laminar Incidence (DLI). *Res Biomed Eng*. 2017;**33**:105. doi:10.1590/2446-4740.05316.
[22] Son DI, Lee JH, Park S. Stress relaxation in free-standing aluminum beams. *Thin Solid Films*. 2005;**476**:124-8. doi:10.1016/j.tsf.2004.10.001.
[23] Schipani F, Villegas EA, Ramajo LA, Parra R. Zinc oxide thin films for a room temperature dual carbon dioxide and carbon monoxide sensor. *J Mater Sci Mater Electron*. 2023;**34**:1092. doi:10.1007/s10854-023-10507-6.
[24] Morari V, Ursaki VV, Rusu EV, Zalamai VV, Colpo P, Tiginyanu IM. Spin-Coating and Aerosol Spray Pyrolysis Processed Zn1−xMgxO Films for UV Detector Applications. *Nanomaterials*. 2022;**12**:3209. doi:10.3390/nano12183209.
[25] Djaaboube H, Mammeri A, Bouachiba Y, Taabouche A, Bouabellou A, Serrar H, Sekhri I. Optical properties and complex refractive index of Co-doped ZnO waveguide thin films elaborated by spray pyrolysis. *J Mater Sci Mater Electron*. 2022;**33**:16056. doi:10.1007/s10854-022-08498-x.
[26] Bouachiba Y, Mammeri A, Bouabellou A, Rabia O, Saidi S, Taabouche A, et al. Optoelectronic and birefringence properties of weakly Mg-doped ZnO thin films prepared by spray pyrolysis. *J Mater Sci Mater Electron*. 2022;**33**:6689. doi:10.1007/s10854-022-07844-3.
[27] Suarez G, Alvira FC, Parra R, Tejerina MR. New Experimental Approaches in Pulsed Laser Deposition: air at atmospheric pressure and multipulse excitation. *OAM-RC*. 2019;**13**:535. doi:10.1364/fio.2019.jw3a.25.
[28] Kim DH, Jang JW, Lee JS. Femtosecond laser bonding of glasses and ion migration in the interface. *J Appl Phys*. 2010;**107**:073528. doi:10.1007/s00339-010-5948-x.
[29] Dey A, Verma N, Raj R. Proton exchange membrane based hydrogen sensor for sodium cleaning application. *Sens Actuators B Chem*. 2013;**182**:215. doi:10.1016/j.snb.2013.03.055.
[30] Sasikala T, Shanmugasundaram K, Thirunavukkarasu P, Chandrasekaran J, Vivek P, Marnadu AR, et al. Characterization of Jet nebulizer spray pyrolysis coated MoS2 thin films and fabrication of p-Si/n-MoS2 junction diodes for optoelectronic application. *Inorg Chem Commun*. 2021;**130**:108701. doi:10.1016/j.inoche.2021.108701.
[31] Park SY, Kang YJ, Lee S, Kim DG, Kim JK, Kim JH, et al. Spray-coated organic solar cells with large-area of 12.25 cm2. *Sol Energy Mater*. 2011;**95**:852. doi:10.1016/j.solmat.2010.10.033.
[32] Sağlam HK, Gür E, Ertuğrul M. Investigation of the growth temperature effect on H2 gas detection for ZnO thin films. *Opt Mater*. 2023;**137**:113521. doi:10.1016/j.optmat.2023.113521.
[33] Falcony C, Aguilar-Frutis MA, García-Hipólito M. Spray Pyrolysis Technique; High-K Dielectric Films and Luminescent Materials: A Review. *Micromachines*. 2018;**9**:414. doi:10.3390/mi9080414.
[34] Toda MJ, El-Shaer A, Atta AM, Ahmed MA. Structural, optical and dielectric investigations of electrodeposited p-type Cu2O. *J Mater Sci Mater Electron*. 2019;**30**:10218. doi:10.1007/s10854-019-02356-z.
[35] Saha JK, Bukke RN, Mude NN, Jang J. Significant improvement of spray pyrolyzed ZnO thin film by precursor optimization for high mobility thin film transistors. *Sci Rep*. 2020;**10**:8999. doi:10.1038/s41598-020-65938-6.
[36] Mariappan R, Ponnuswamy V, Ragavendar M. Influence of molar concentration on the physical properties

of nebulizer-sprayed ZnO thin films for ammonia gas sensor. *Mat Sci Semicon Proc*. 2013;**16**:1328. doi:10.1016/j.mssp.2012.10.012.
[37] Ramos C, Alarcón J, Quintana M, Rodríguez J, Estrada W. Ectoparásitos en aves del género Agapornis en cautiverio en La Habana, Cuba. *Rev Soc Quím Perú*. 2008;**48**:282. doi:10.15381/rivep.v29i3.14767.
[38] Guillemoles JF, Linncot D, Cowache P, Vedel. Solvent Effect on ZnO Thin Films Prepared by Spray Pyrolysis. *10th European Photovoltaic Solar Energy Conference and Exhibition*, Lisboa, Portugal; 1991. doi:10.1007/978-94-011-3622-8_156.
[39] Hazmin SN, Mamat MH, Muhamad NA. Effect of nozzle-substrate distance on the structural and optical properties of AZO thin films deposited by spray pyrolysis technique. *AIP Conf Proc*. 2021;**2332**:120001. doi:10.1063/5.0043397.
[40] Rajalekshmi ES, Raj AME. Effect of substrate temperature on structural and morphological studies by spray pyrolysed ZnO thin films. *Solid State Commun*. 2021;**338**:1114479. doi:10.1016/j.ssc.2021.114479.
[41] Chebil W, Boukadhaba M, Fouzri A. Epitaxial growth of ZnO on quartz substrate by sol-gel spin-coating method. *Superlattices Microstruct*. 2016;**95**:48. doi:10.1016/j.spmi.2016.04.033.
[42] Kuech TF. Thin Films and Epitaxy: Materials, Processes, and Technology. *Handbook of Crystal Growth*, Vol. III. Elsevier; 2015. doi:10.18240/ijo.2024.04.25.
[43] Şimşek B, Ceran ÖB, Şara ON. Difficulties in Thin Film Synthesis. In: Kharissova OV, Torres-Martínez LM, Kharisov BI, eds. *Handbook of Nanomaterials and Nanocomposites for Energy and Environmental Applications*. Springer, Cham; 2021. doi:10.1007/978-3-030-36268-3_84.
[44] Deshmukh T, Dzade NY. Spray Pyrolysis: Thin Film Coating. In: Sankapal BR, Ennaoui A, Gupta RB, Lokhande CD, eds. *Simple Chemical Methods for Thin Film Deposition*. Springer, Singapore; 2023. doi:10.1007/978-981-99-0961-2_8.
[45] Kwon T, Ohnishi T, Mitsuishi K, Ozawa TC, Takada K. Synthesis of LiCoO2 epitaxial thin films using a sol–gel method. *J Power Sources*. 2015;**274**:417. doi:10.1016/j.jpowsour.2014.10.070.
[46] Villegas EA, Aldao CM, Savu R, Ramajo LA, Parra R. Effects of Grain Size on the UV-Photoresponse of Zinc Oxide Thin Films Grown by Spray-Pyrolysis. *Phys Status Solidi A*. 2018;**215**:1800107. doi:10.1002/pssa.201800107.
[47] Viezbicke BD, Patel S, Davis BE, Birnie DP. Evaluation of the Tauc method for optical absorption edge determination: ZnO thin films as a model system. *Phys Status Solidi B*. 2015;**252**:1700. doi:10.1002/pssb.201570351.
[48] Aebersold AB, Fanni L, Hessler-Wyser A, Nicolay S, Ballif C, Hebert C, Alexander DTL. Quantifying competitive grain overgrowth in polycrystalline ZnO thin films. *Acta Mater*. 2019;**173**:74. doi:10.1016/j.actamat.2019.04.049.
[49] Znaidi L. Sol-gel-deposited ZnO thin films: A review. *MSEB*. 2010;**174**:18. doi:10.1016/j.mseb.2010.07.001.
[50] Santos AMP, Santos EJP. High quality c-axis oriented thin ZnO film obtained at very low pre-heating temperature. *Mater Lett*. 2007;**61**:3432-5. doi:10.1016/j.matlet.2006.11.084.
[51] Dorranian D, Dejam L, Mosayebian G. Optical characterization of Cu3N thin film with Swanepoel method. *J Theor Appl Phys*. 2012;**6**:13. doi:10.1186/2251-7235-6-13.
[52] Muslimov AE, Tarasov AP, Kanevsky VM. Interference Phenomena and Stimulated Emission in ZnO Films on Sapphire. *Materials*. 2022;**15**:6409. doi:10.3390/ma15186409.
[53] Benkhetta Y, Attaf A, Saidi H, Messemeche R, Bouhdjer A, Bendjedidi H, et al. Controlling of c-axis position of ZnO nano-crystalline films deposited at various substrate temperature by ultrasonic spray method. *Brit Cer Pr*. 2020;**21**:100698. doi:10.1016/j.surfin.2020.100698.
[54] Singh P, Kumar A, Deepak, Kaur D. Growth and characterization of ZnO nanocrystalline thin films and nanopowder via low-cost ultrasonic spray pyrolysis. *J Cryst Growth*. 2007;**306**:303. doi:10.1016/j.jcrysgro.2007.05.023.
(Rec. 14/11/2023, Rev. 12/05/2024, Ac. 25/09/2024) (AE: D. Z. de Florio)

Appendix A. Video frames of ZnO film growth nebulized stages.